ELSEVIER

NeuroImage

www.elsevier.com/locate/ynimg
NeuroImage 26 (2005) 330–346

Contrast response in visual cortex: Quantitative assessment with intrinsic optical signal imaging and neural firing

Chang'an A. Zhan,[a,*] Timothy Ledgeway,[a,b] and Curtis L. Baker Jr.[a]

[a]*Department of Ophthalmology, McGill Vision Research, McGill University, 687 Pine Avenue West, H4-14, Montreal, QC, Canada H3A 1A1*
[b]*School of Psychology, University of Nottingham, UK*

Received 23 February 2004; revised 18 January 2005; accepted 31 January 2005
Available online 16 March 2005

While previous studies showed that intrinsic optical signals spatially correspond with electrophysiological responses in mammalian visual cortex, the quantitative correspondence of their response strengths is open to question. Measurement of both signals' strength as functions of visual stimulus contrast provides an opportunity for quantitative comparison. Towards that end, the spatial and temporal properties of the optical signal impose important constraints upon quantification of its strength. We used intrinsic optical signal imaging and single unit recording to measure responses to drifting gratings at contrasts ranging from 10–80% in cat area 18. We calculated the average difference images for pairs of oppositely moving, or orthogonally oriented, gratings at each contrast and evaluated three different methods for quantifying optical signal strength. After about 2.5 s, the spatial patterns of optical images and the time course of their strength were contrast-invariant. This "space–time-contrast separability" for optical response implies a spatial uniformity of the optical contrast response functions, provides an objective basis to guide temporal averaging of optical signals, and validates a scalar metric of optical signal strength. Optically measured contrast response functions increase monotonically and saturate at high contrasts, qualitatively resembling those from single units. However, quantitative comparison reveals a nonlinear relationship with neural firing, such that the optical response reaches half of its maximum when the neural response has reached only around 20% of its maximum. This relationship suggests that intrinsic optical signals are relatively more sensitive to weak signals than neural firing.

Keywords: Contrast response function; Orientation selectivity; Direction selectivity; Visual cortex; Cortical map; Optical imaging

Introduction

Intrinsic optical signal imaging measures local activation-related changes in light reflected from neural tissue (for review, see Blasdel, 1997; Grinvald et al., 1999). While this functional imaging was validated by electrophysiology (Shmuel and Grinvald, 1996), supporting an implicitly accepted view that the former represents neural firing rates, the indirect nature of the optical signal raises questions of its quantitative relation to neural activity and the coupling mechanism. To resolve these issues requires a better understanding of the spatial and temporal properties of the optical signals and of how to appropriately quantify their magnitude. Similar issues have been of recent interest for blood-oxygenation-level-dependent (BOLD) fMRI where a quantitative understanding of the relationship is also crucial for interpreting imaging results functionally (e.g., Logothetis et al., 2001; Rees et al., 2000). Because the intrinsic optical signal is hemodynamically driven and reflects oxygenation (Malonek and Grinvald, 1996), its relationship to neural firing may also be relevant to the interpretation of fMRI signals.

Previous efforts to compare neuroimaging with electrophysiology have concentrated on their spatial correspondence, for optical imaging, or response strengths, for fMRI. Shmuel and Grinvald (1996) and Masino (2003) demonstrated that optical signals are spatially correlated with electrical activity. Thompson et al. (2003) found correlated changes of local oxygenation and neural firing. A linear proportionality between monkey neuron firing rates and human fMRI strength was reported by Heeger et al. (2000) and Rees et al. (2000) for varying grating contrast or random-dot motion coherence, respectively. However, Logothetis et al. (2001), recording simultaneously the response to a series of contrast stimuli from monkey V1, showed that fMRI is quite nonlinearly related to multi-unit firing. This nonlinearity might arise from a disproportionate contribution of metabolic demands and/or sub-threshold activity (Das and Gilbert, 1995; Toth et al., 1996) to imaging signals.

The visual cortex of the cat (Payne and Peters, 2002) affords a good opportunity to quantitatively compare optical imaging and neural firing—it is rich in neurons selective for orientation and direction of motion, columnar organization of both properties has been revealed by optical imaging (Shmuel and Grinvald, 1996; Weliky et al., 1996) as well as electrophysiology

* Corresponding author. Fax: +1 514 843 1691.
E-mail address: changan.zhan@mcgill.ca (C.A. Zhan).
Available online on ScienceDirect (www.sciencedirect.com).

1053-8119/$ - see front matter © 2005 Elsevier Inc. All rights reserved.
doi:10.1016/j.neuroimage.2005.01.043

(Swindale et al., 1987), and the contrast response functions (CRFs) of single units have been extensively studied (e.g., Albrecht et al., 2002; Bonds, 1991). Therefore, in this preparation, it is feasible to compare differential responses to opposite directions of motion, or orthogonal orientations, in a parallel manner for optical signals and for neurophysiology, as functions of contrast.

We have recorded and systematically quantified CRFs for orientation and direction selectivity by both optical imaging and single unit recording in cat A18. The spatial patterns of optical images and the time course of optical signal strength are contrast-invariant, implying a "space–time-contrast separability" of the optical signals. This property implies a spatial uniformity of the optical contrast response function, provides an objective basis to guide temporal averaging of the optical signals, and validates a scalar metric of optical response strength. Both optical imaging and electrophysiological CRFs are monotonically increasing functions, but the former saturates at lower contrasts. These results suggest that hemodynamically driven imaging signals are relatively more sensitive to weak signals when measured using a differential protocol and represent a more complex signature of neural activity than simply neural firing. Some aspects of this work have been described in abstract form (Zhan et al., 2002).

Materials and methods

Animal preparation and maintenance

The surgical and life support procedures were similar to those described elsewhere (Mareschal and Baker, 1999) and were approved by the institutional Animal Care Committee. Briefly, adult cats were initially anesthetized with halothane/oxygen, a venous cannula was inserted, and i.v. atropine (0.8 ml) and dexamethasone (0.12 ml) administered. Subsequent surgical anesthesia was obtained with i.v. sodium pentothal as required. During surgery, the corneas were protected with topical methylcellulose. Following tracheal cannulation, the animal was secured in a stereotaxic apparatus. A craniotomy (6 × 8 mm for optical imaging, 3 × 3 mm for electrophysiology) was centered at Horsley-Clark coordinates A3/L4 to expose the crown of the medial gyrus containing the lower hemifield representation of area 18 (Tusa et al., 1979). For optical recording, the dura was carefully removed and a plastic chamber attached to the skull with dental acrylic. The craniotomy was covered with 2% agarose; for optical imaging, the chamber was sealed with a cover slip. After completion of surgery, the animal was paralyzed with 4 mg/kg flaxedil (gallamine triethiodide) and artificially respired with oxygen/nitrous oxide. Atropine (1%) and phenylephrine hydrochloride were used to paralyze accommodation and retract the nictitating membranes. The corneas were protected with gas permeable contact lenses. The eyes were focused on a tangent screen at a distance of 28.5 cm (optical imaging) or 57 cm (electrophysiology); in addition to artificial pupils (D = 2.5mm), appropriate spectacle lenses were selected using streak retinoscopy. Throughout the experiment, the animal was infused with 10 mg/(kg-h) flaxedil and 1 mg/(kg-h) pentobarbital sodium in lactated dextrose ringers. A thermistor-controlled heating pad was used to maintain the body temperature at about 37.5°C. The physiological state and anesthesia level of the animal were constantly monitored (EEG, ECG, expired CO2, temperature, blood oxygen level, and heart rate) and maintained at appropriate levels.

Visual stimuli

Visual stimuli were computer-generated (Macintosh G4, 1GHz, 1GB RAM) using custom software written in Matlab (The MathWorks) and Psychophysics Toolbox (Brainard, 1997; Pelli, 1997) and displayed on a NEC Multisync FP1350 monitor (screen nonlinearity gamma-corrected), as described previously (Mareschal and Baker, 1999). For optical imaging, a larger field size was achieved by using a short viewing distance of 28.5 cm (screen resolution, 1024 × 768, refresh rate, 85Hz); stimuli consisted of drifting sine- or square-wave gratings, with spatial and temporal frequency at 0.15 cpd and 4 Hz respectively, which are appropriate for neurons in cat A18 (Issa et al., 2000; Movshon et al., 1978; Zhou and Baker, 1996).

Fig. 1 illustrates example visual stimuli and the timing of optical data acquisition. To obtain a direction map, vertical gratings were drifting left or right (Fig. 1A). To map orientation selectivity, gratings were oriented horizontally or vertically (Fig. 1B) with direction of motion alternating every 3 cycles. A visual stimulus was presented for 8 s, with prior (6.4 s) and following (3.7 s) periods for optical recording (see below), and a 15 s inter-trial interval (Fig. 1C). The beginning of frame acquisitions was initiated by the visual stimulus computer and was not synchronized with cardiac or respiratory cycles. In the absence of grating stimuli, the screen was always maintained at the average gray level to prevent luminance transients.

For single unit recording, the viewing distance was 57 cm (screen resolution 640 × 480, refresh rate 75Hz). Except as noted, grating parameters were optimized for each neuron, and gratings were presented 3 s for each trial.

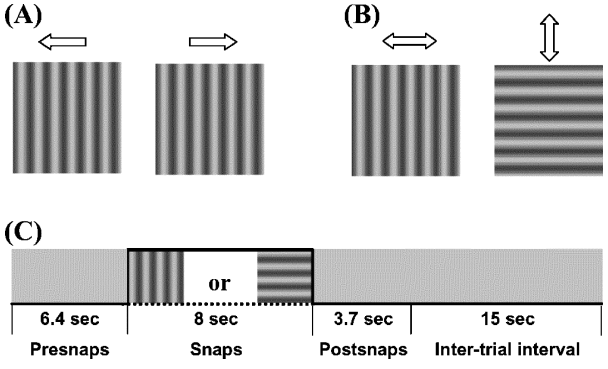

Fig. 1. Visual stimuli and timing of optical data acquisition. (A) Example visual stimuli for direction selectivity measurement: vertical gratings at four contrasts (10%, 20%, 40%, and 80%), spatial frequency of 0.15 cpd, and temporal frequency of 4 Hz, drifting left or right. (B) Example visual stimuli for orientation selectivity measurement, horizontally or vertically oriented gratings drifting alternately in two directions perpendicular to their orientations. Contrast levels and spatial and temporal frequency were the same as for directional visual stimuli. (C) Optical data collection lasted about 18 s for each trial: 6.4 s before the onset (Presnaps), 8 s visual stimulation (Snaps), 3.7 s post-stimulus (Postsnaps); a 15 s inter-trial interval was used to reduce effects of visual adaptation and response residual from the previous trial.

Optical imaging system calibration and data acquisition

The exposed brain surface was illuminated with 8 light-emitting diodes (LEDs, supra-bright, 720 nm) on a stabilized DC power source, and its image was brought to a CCD camera (Cohu 4812, 56dB) by a macro zoom lens (f2.5, 18–108 mm) focused below the cortical surface. Timing signals from the visual stimulus computer controlled a digital video processor (DVP-32, InstruTech, NY), which digitized the video signals (12 bits) and provided real-time temporal averaging and spatial binning. The raw image data (640 × 480 pixels, 30 frames per second) were averaged into 16-bit 320 × 240 images (spatial binning ×2) at ca. 2 frames per second (temporal binning ×16), and transferred to a RAID disk (360GB) on the DVP-32 host computer (PIII, 800 MHz, 512 MB RAM) for off-line analysis.

The LEDs were positioned to provide a uniform illumination and the lens aperture and/or LED brightness adjusted to ensure that image intensity levels spanned the full linear range of the CCD camera. Vibration stability was provided by an air table (TMC, Massachusetts), and a black shroud was positioned to block stray light.

Usually about 15–30 repetitions were recorded for orientation and 30–45 for direction selectivity imaging sessions. A typical session of 30 repetitions of a set of 8 conditions (4 Michelson contrasts, 10%, 20%, 40% and 80%; 2 directions/orientations) required about 2 h of recording time and resulted in about 2.4 GB of data files, initially stored on the RAID hard disk, and later archived to DVD-R media.

Electrophysiology

Some of these recordings were obtained as part of a detailed study of single unit contrast response for direction selectivity in cat area 18 (Ledgeway and Baker, 2001). Single unit recording procedures were conventional and have been described in detail elsewhere (Mareschal and Baker, 1999). The depth of each recorded neuron was measured with reference to the cortical surface, which was roughly estimated from multiunit activity detected on the audio monitor. A series of quantitative measurements were used to find each neuron's optimal sinewave grating (position, size, orientation, direction, and spatial and temporal frequency). In the main experiment, the optimal gratings were presented at the same series of contrasts as for optical imaging. Average spike frequencies to two opposite directions of motion, preferred (P) and non-preferred (NP), were recorded; as a rough scalar index of a neuron's directionality, a direction selectivity index (DSI) was calculated as DSI = (P − NP) / (P + NP), averaged across the four contrast conditions. Similarly, average spike frequencies to gratings at the preferred orientation (P) and its orthogonal orientation (NP) were recorded, and a scalar index of orientation selectivity (OSI) calculated by the same formula. A population average direction- or orientation-selective contrast response function was estimated by pooling P − NP values from all neurons producing a DSI or OSI greater than 0.1.

Image data processing

Optical data were post-processed with custom software, implemented in Matlab and C language mex functions, using conventional methods (Blasdel, 1997; Grinvald et al., 1999). The first step was to correct for uneven illumination by dividing each image by the averaged Presnaps images. These corrected images were then averaged across repetitions for each stimulus condition at each time point to increase the signal-to-noise ratio while retaining temporal information. Fig. 2A shows an example raw optical image, which contains blood vessels, edges of skull, and uneven illumination. Based on a preliminary difference image (orthogonal orientations at the highest contrast), an ROI with arbitrary geometry (indicated by the inner polygon in Fig. 2A) was manually defined for the most visually responsive region. To increase image contrast, the intensity range of the raw image within the ROI was linearly expanded to the whole gray level range (Fig. 2B).

The next step was to calculate difference image time series for pairs of opposite directions of motion or for orthogonal orientations. While blood vessel signals were greatly reduced by differencing the averaged images for each pair of conditions, their residual was not negligible (Fig. 2C), and warranted removal by a segmentation and masking procedure. Raw and difference images (Figs. 2B and C, respectively) were high-pass filtered and binarized to extract their blood vessel patterns (manual intervention applied when necessary); then these segregated blood vessel patterns within the ROI were pooled by taking their union to provide a blood vessel pattern mask for each dataset. This mask was then applied to each frame of the difference images (Fig. 2D).

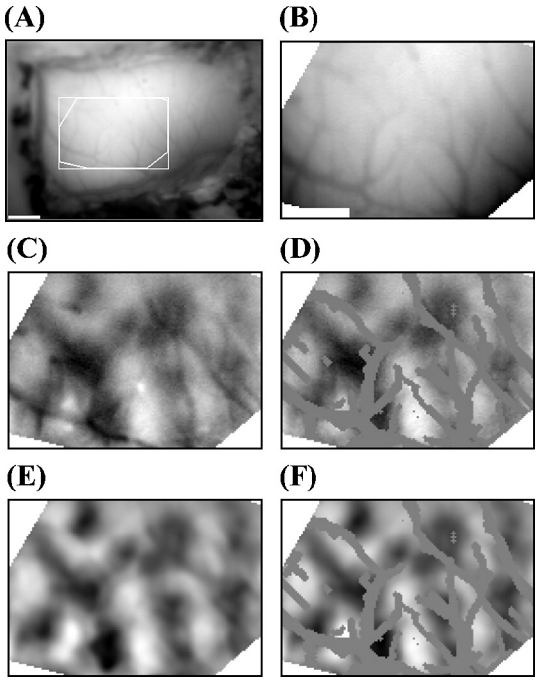

Fig. 2. Image preprocessing. (A) Raw image shows edges of craniotomy, uneven illumination, and blood vessels. The white rectangle indicates the bounding-box of the region of interest (ROI, inner 8-sided polygon); scale bar, 1 mm. (B) Raw image (intensity range linearly expanded within the ROI); scale bar, 1 mm, applicable to panels B–F. (C) Raw orientation difference-image within the ROI. (D) Raw difference-image with blood vessel masking. (E) Interpolated and band-pass filtered (see text for details) difference-image. Masking and interpolation prevent strong blood vessel artifact from contaminating the pixels in vessel free zones during image filtering. However, only data from vessel free zones are used for further quantitative analysis. Panel (F) shows these blood vessel free zones (within ROI and beyond the blood vessel masks).

In addition to blood vessel artifacts, raw difference images are subject to artifacts at low spatial frequencies, induced by respiratory and cardiac fluctuations, and inhomogeneous blood diffusion (e.g., vasomotion); and high spatial frequency noise arises from the CCD camera, electrical sources, and digitization, which also degrades image quality. Therefore, both high- and low-pass spatial filtering (with appropriate cutoff parameters—see below) were employed. However, if filtering were simply applied to the masked image (Fig. 2D), it would introduce artifacts from the sharp edges formed by the blood vessel masks; if the filtering were applied to the unmasked image (Fig. 2C), large artifacts from blood vessels would contaminate neighboring pixels. To avoid this problem, the filtering was applied to images in which the masked regions were interpolated from weighted averages of nearby pixels in blood vessel free areas (Fig. 2E); then the mask was re-applied to the filtered images (Fig. 2F) for subsequent data analysis.

The low-pass filtering was achieved by convolution with a Gaussian kernel (σ = 3 pixels, about 75 μm). To implement high-pass filtering, the lowest spatial frequencies were extracted by convolution with a Gaussian kernel, σ = 30 pixels, about 750 μm), and this low-pass image was then subtracted from the original image. These filter parameters were effective in removing the fine-grain noise and coarse-scale intensity gradients, while having minimal effect on genuine orientation- or direction-domains. This final processed image, after re-applying the blood vessel pattern mask, is shown in Fig. 2F, revealing a typical quasi-periodic, patchy response pattern similar to those reported previously (Shmuel and Grinvald, 1996; Weliky et al., 1996). Only pixels from blood vessel free zones were subsequently used for quantitative evaluation.

Quantification of optical response strength

Fig. 3A shows time-averaged orientation difference images to 5 visual stimulus contrasts (blank, 10%, 20%, 40%, and 80%, from top to bottom; see below and Fig. 6 for details on the time window for temporal averaging based on the results from basic image processing shown in Fig. 2), where the 4 images to 10–80% contrasts are shown at the same intensity scale and the blank response is shown with 20 times greater scale. Each stimulus-driven difference image was calculated by subtracting the average image to horizontally oriented drifting gratings from the average image to vertically oriented drifting gratings; therefore the light and dark regions show response to horizontal and vertical gratings, respectively. The blank response was calculated from an average of differences of pairs of images collected during the "Presnaps" periods (Fig. 1C) preceding the visual stimulus.

The stimulus-driven difference images show a progressively increasing prominence of light and dark regions with increasing stimulus contrast, suggesting that response strength might be quantified by measuring the dispersion of pixel values in each image. In all the subsequent quantitative assessment of optical signal strengths, we only used the pixel values from blood vessel free zones. Fig. 3B shows corresponding image pixel value histograms, which verify that pixel values span a systematically broader range with increasing visual stimulus contrast (note expanded abscissa scale for blank condition). However, a scalar response metric based simply on image pixel value dispersion is a valid response measure only if the spatial pattern of response does not change with contrast and the response strength to the blank condition (which is actually noise) is negligible (see Appendix).

The spatial patterns for the stimulus-driven difference images in Fig. 3A appear very similar, while the pattern to the blank screen shows only much lower amplitude, grainy noise (note expanded intensity scale). This impression was quantified by correlation analysis. As shown in Fig. 3C, the visual stimulus-driven pixel values in blood vessel free zones within the ROI are highly correlated with those to 80% contrast (correlation coefficient greater than 0.9); whereas the image pattern to the blank screen shows a very small correlation coefficient (smaller than 0.1), reflecting the lack of stimulus-driven response. This result indicates quantitatively that the spatially differentiated intensity regions of the stimulus-driven images are highly reproducible visual responses rather than spurious noise and provides a necessary condition for the validity of an intensity dispersion response metric.

Because the stimulus-driven response images are highly correlated, it can be shown that their pixel value histograms must be of similar shape (see Appendix). This prediction is supported by the pixel value histograms shown in Fig. 3B, each of which could be fit with Gaussian functions ($r^2 > 0.9$). The blank response histogram was also well-fit by a Gaussian, though of much narrower width. Thus, a useful response metric is the standard deviation (SD) of the intensity histogram's best-fitting Gaussian—the stronger the optical response, the larger the SD of the pixel value dispersion (Schuett et al., 2001).

In the case of a small ROI, the energy in light and dark regions is unequal, and the image intensity histogram is non-Gaussian (as also sometimes seen in fMRI—Hanson and Bly, 2001); therefore the standard deviation of the image intensity is not appropriate in characterizing the optical signal strength. In this case, an alternative measure is the interquartile range (IQR) of the image pixel values. This measure was calculated by taking the difference between the 25 percentile and 75 percentile response levels in the image pixel value histogram.

While the SD and IQR methods provide statistical characterizations of response amplitudes, they do not reveal region- or pixel-wise information. For example, we need to investigate whether contrast response functions in optimally activated regions are different from those in sub-optimally activated regions. Optimally activated regions are formed by pixels with the largest values (peak for horizontal stimuli) and smallest values (trough for vertical stimuli); sub-optimally activated regions are formed by pixels with medium-large values (for horizontal stimuli) and medium-small values (for vertical stimuli). To segregate the images into different sub-regions, firstly we normalized optical responses to the 10–40% conditions into the same range as that to the 80% condition and averaged these images (Fig. 3D); a pixel value histogram (Fig. 3E) of the averaged image was then partitioned into 5 pixel value levels (separated by dashed vertical lines) having an equal number of pixels for each level. Pixels within each value level were segregated into each sub-region (color-coded in Fig. 3F). Regions in red and blue were optimally stimulated by horizontal and vertical visual stimuli, respectively, and formed the first peak–trough pair (PT1); regions in orange and cyan were sub-optimally stimulated and formed the second peak–trough pair (PT2). Pixels in green regions had values close to zero and thus were not used for peak–trough analysis.

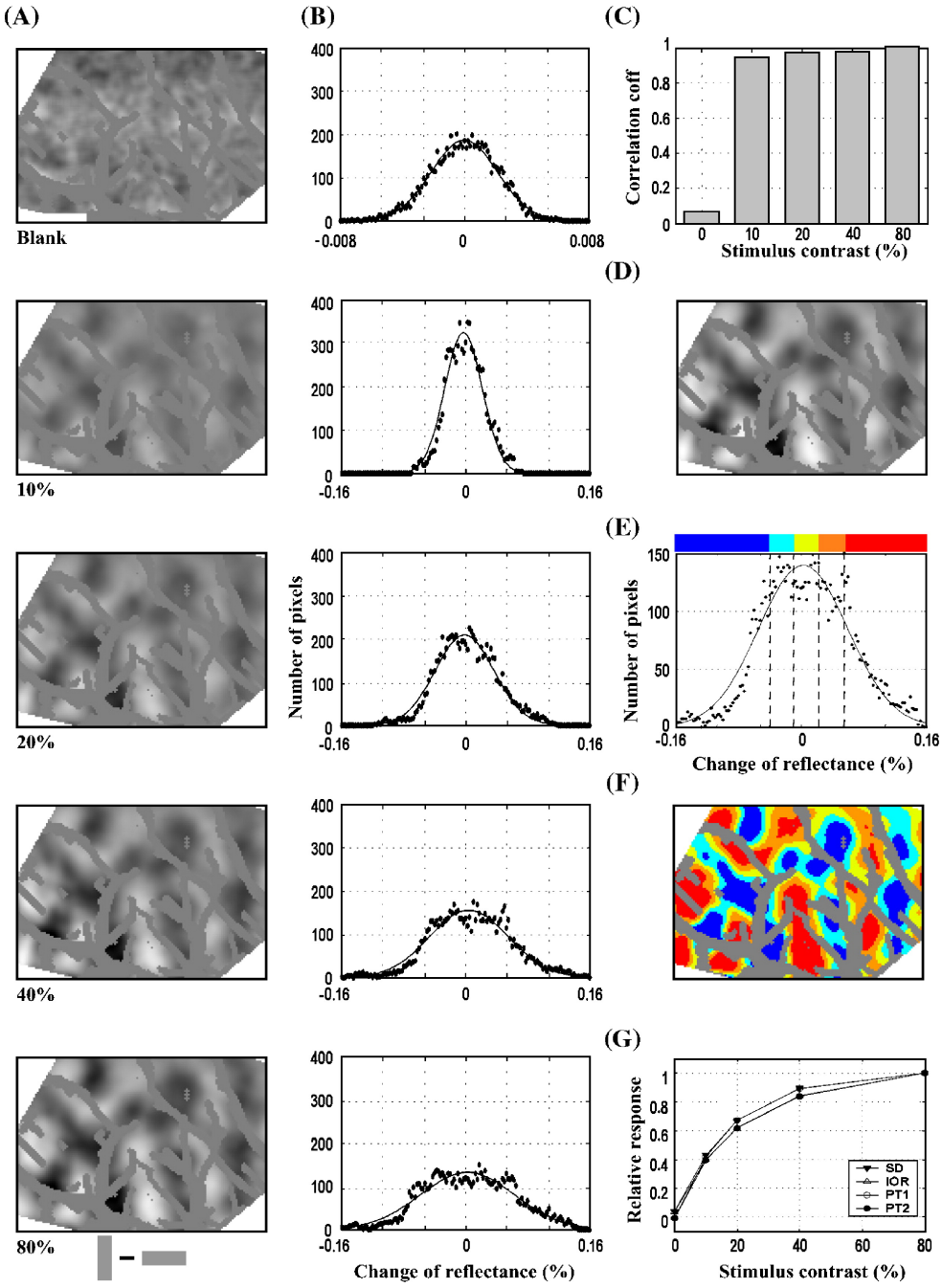

Fig. 3. Quantification of optical response strengths to orientation stimuli. (A) Time-averaged orientation difference-images for vertical vs. horizontal gratings, for 5 visual stimulus contrasts (blank, 10%, 20%, 40%, and 80%, from top to bottom). The four images to 10–80% contrast are shown at the same intensity scale, while the image to the blank screen is 20 times additionally amplified. Because increased neural activity corresponds to decreased reflectance, the darker regions of the difference-image correspond to stronger responses to vertical orientation. Subsequent analysis uses only pixels from blood vessel free areas. (B) Response strength histograms (number of pixels vs. $\Delta R/R$, reflectance levels). The dispersion of pixel values, which indicates the optical response amplitude, was quantified as the standard deviation (SD) of the best-fitting Gaussian. An alternative measure of intensity dispersion is the interquartile range (IQR), which takes the difference between the upper and lower 25 percentile intensity levels. (C) Spatial correlation coefficients of image patterns within the ROI, with respect to the image response for 80% contrast. Visual stimulus-driven responses are highly correlated with one another, whereas the image pattern to the blank screen is not because it contains little stimulus-driven response. (D) Composite difference-image calculated as weighted average of optical difference-image responses to 10–80% contrast visual stimuli. (E) Histogram of pixel values from blood vessel free zones in image D, with best-fitting Gaussian. Histogram has been partitioned into 5 subsets according to pixel values (indicated by dashed lines and different colors), with each subset containing 20% of the total pixels. (F) Composite difference map as in panel D, in which blood vessel free zones were partitioned into 5 sub-regions according to pixel values, with color-mapping as in panel E. "Peak–trough" contrast response functions were calculated from the difference between the maximally responsive sub-regions (PT1—blue for vertical orientation, red for horizontal) or between sub-maximally responsive sub-regions (PT2—cyan for vertical and orange for horizontal) at each stimulus contrast level. (G) Normalized response strengths to 5 contrasts of visual stimuli, evaluated by standard deviation (SD), interquartile range (IQR), and peak–trough difference (PT1 and PT2).

Fig. 3G shows resulting contrast response functions, normalized to the highest response amplitude, evaluated by different methods. SD and IQR represent the results from standard deviation and interquartile range methods; PT1 and PT2 are evaluated from the maximally and sub-maximally responsive pixel values, respectively. While the absolute response amplitudes estimated by these methods differ in magnitude, their normalized contrast response functions are highly similar (Fig. 3G). Because the blank condition responses are very small compared to those for tested contrasts, all the contrast functions are normalized to vary from zero to unity.

The above analysis was performed on filtered images, as described earlier—although image filtering is commonly used to improve optical signals (e.g., Issa et al., 2000; Shmuel and Grinvald, 1996; Weliky et al., 1996), we need to understand its impact on response quantification. Fig. 4 illustrates the analysis of

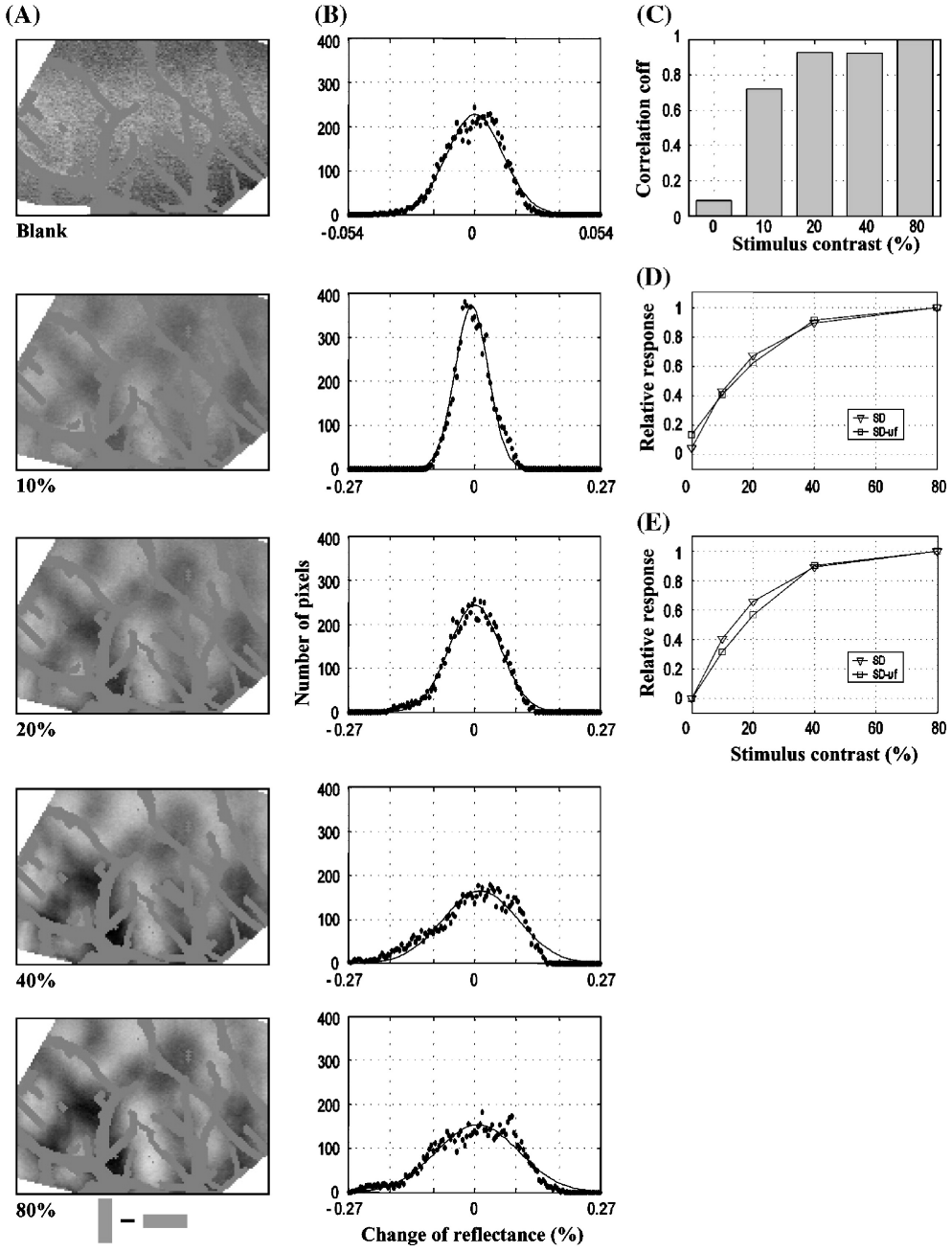

Fig. 4. Quantification of optical response strength with unfiltered data. (A) Time-averaged orientation difference-images corresponding to those in Fig. 3A, but without spatial filtering. (B) Response histograms as Fig. 3B for the images in panel A, with Gaussian curve-fits. The unfiltered data span broader ranges, especially for the blank condition (note 5-fold expanded abscissa scale, rather than 20-fold as in Fig. 3B). (C) Correlation coefficients between stimulus-driven responses and maximal response (to 80% contrast condition)—note the substantially decreased values for the 10–40% conditions compared to those in Fig. 3C. (D) Contrast response functions evaluated from the filtered data (△) and unfiltered data (□). Unfiltered data give significant positively-biased response strength for the blank condition, which should be zero. (E) Contrast response functions as in panel D but normalized into a range between zero and one. Note that the larger bias for unfiltered blank response now drags the contrast response function downwards.

unfiltered optical responses, for the same dataset as in Fig. 3. The temporally-averaged orientation maps (Fig. 4A) contain more high frequency noise than those in Fig. 3A, reflecting the absence of low-pass filtering. The images also contain very low frequency components (due to the lack of high-pass filtering), whose low amplitude renders them most visible in the blank condition. When these unfiltered images are analyzed for their signal strengths, their pixel value histograms (Fig. 4B) span larger ranges than those in Fig. 3B. Especially for the blank condition, the unfiltered data span about a 7-fold broader range of values than in the presence of filtering. Fig. 4C shows correlation coefficients between optical responses, which are now significantly smaller compared to those for filtered data (Fig. 3C)—note that the degradation is most serious for the lower signal strengths. Fig. 4D compares the contrast response functions from filtered data (triangles, as in Fig. 3G) and unfiltered data (squares). With the highest values normalized to unity, the response strengths for stimulus-driven conditions are comparable, but the estimate for the blank condition is much more positively biased for unfiltered than for filtered data. If we normalize the data into a zero-to-unity range (Fig. 4E), the large positively biased blank response drags the relative responses for the 10% and 20% conditions downwards, distorting the contrast

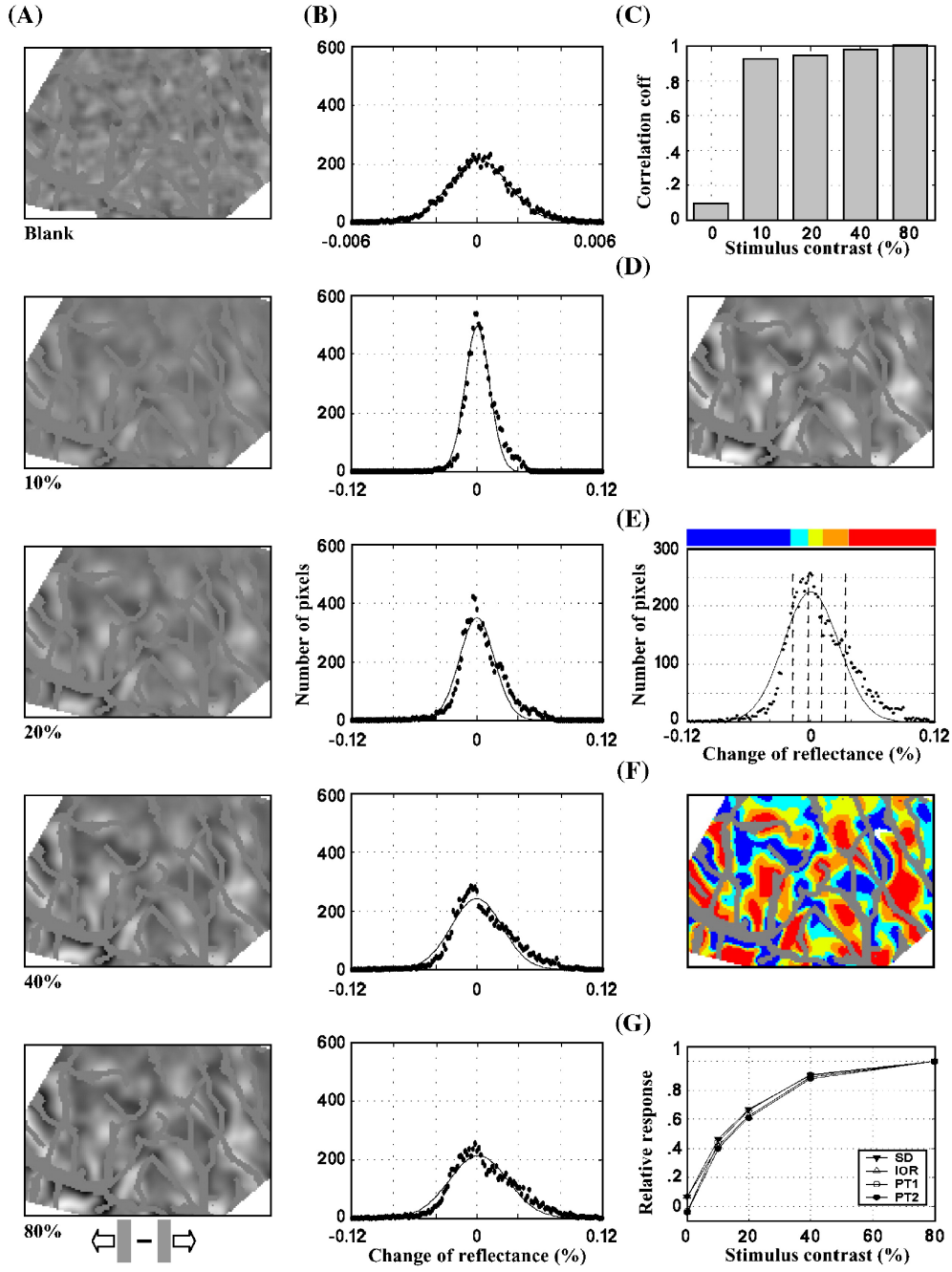

Fig. 5. Quantification of optical response strengths to direction stimuli. Same analysis as in Fig. 3, applied to optical responses to direction stimuli. Darker regions correspond to stronger response to leftwards drifting vertical stimuli; brighter regions correspond to stronger response to rightwards drifting vertical stimuli.

response function shape. Thus, in the absence of filtering, the results are broadly similar, but the quantitative analysis suffers from degraded reliability for weaker signals, and a significant bias is exerted upon the estimated blank response. These effects would in turn result in distortions of contrast response functions and the scalar descriptors (Naka–Rushton curve-fit parameters, see below) used to compare them. Because neural orientation tuning is contrast invariant (e.g., Albrecht and Hamilton, 1982; Anderson et al., 2000; Sclar and Freeman, 1982) and optical signals are spatially well-correlated to neuronal activity (Shmuel and Grinvald, 1996), the correlation coefficients in Fig. 4C for low contrast conditions should be also high; because the differential maps for the blank condition do not contain any response, their amplitudes should be zero. The Appendix section provides a more formal development of how noise can distort image correlations and bias blank responses. Therefore, we conclude that the use of spatial filtering, with appropriately chosen filter parameters, is highly advantageous for our quantitative analysis.

The same procedures as illustrated in Fig. 3 were also applied to analyze optical imaging data for direction selectivity. Fig. 5A shows difference maps for direction of motion for five stimulus contrasts, and Fig. 5B shows their corresponding pixel value histograms. Again, the spatial patterns of stimulus-driven responses were highly correlated (Fig. 5C). Partitioning of responses into response-strength sub-regions for peak–trough analysis (Figs. 5D–F) was done in an analogous manner as for orientation maps. Contrast response functions for direction-maps using SD, IQR, and peak–trough difference methods (Fig. 5G) were again very similar.

Except as indicated, the SD method was subsequently used for quantifying optical responses. Statistical tests of significance, both for optical and neural responses, employed the Student's t test; differences were reported as significant for P values below 0.01.

Results

The quality of recorded imaging data was assessed by the time courses of "inter-contrast correlation" analysis of the orientation- or direction-difference images, as described below. Datasets with highly correlated stimulus-activated response frames were used for further evaluation of the contrast response functions. We found it more difficult to obtain high quality direction maps than orientation maps, consistent with previous reports that direction signals are relatively weaker (Bonhoeffer and Grinvald, 1993; Shmuel and Grinvald, 1996). Optical imaging data included in this study were collected from 8 cats; 18 datasets were used for orientation-difference images and 4 datasets for direction-difference images. Single unit recordings were collected from 58 neurons.

Dynamics and contrast-invariance of intrinsic optical response

Conceivably, the strength of intrinsic optical response and its spatial pattern might change over the time course of response in a

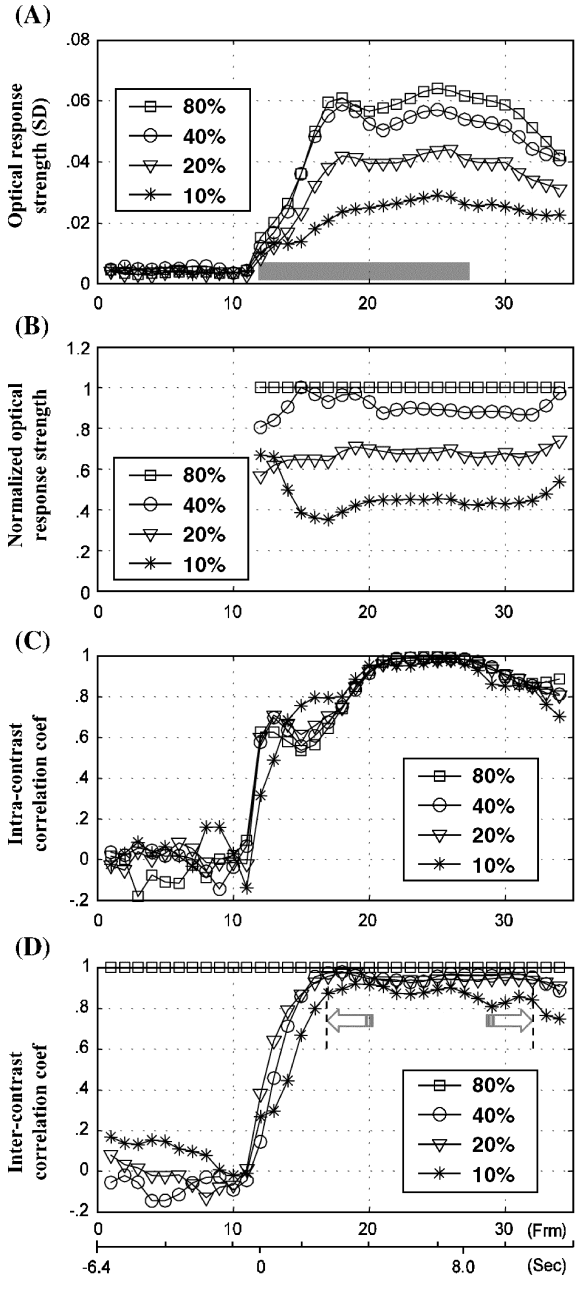

Fig. 6. Time course analysis of the intrinsic optical response. (A) The time courses of optical responses to 4 visual stimulus contrasts estimated from orientation difference-images by the SD method. The gray bar indicates the duration of visual stimuli (8 s, same for all panels). (B) The time course of normalized response amplitudes showing relative response strength. At each time point, responses to four contrasts were normalized by the response to the maximal contrast (80%). About 2.5 s after the onset of visual stimuli, relative response strength achieved a quite stable level for each contrast (note that values prior to stimulus onset will have excessive variance due to division by very small noisy responses—hence they are not plotted here). (C) The time course of the "intra-contrast correlation" coefficient, to examine the spatial pattern dynamics of the optical responses. For each contrast condition, the 20th–27th frames were averaged as a standard template and each frame for that condition was correlated with this template. (D) The time course of the "inter-contrast correlation" coefficient, to examine the optical response pattern's contrast-invariance. At each time point, the image to 80% contrast was used as a correlation template for the responses to other contrasts. Following stimulus onset, the correlation coefficients increased rapidly and maintained high values. Comparing the "intra-contrast" and "inter-contrast correlation" analyses, the optical response patterns shown here were relatively contrast-invariant over a time window of the 17th–32nd frames (indicated by the pair of arrows).

way that could complicate the measurement of their contrast dependence. Therefore, we investigated the time dependence of response strength and spatial pattern based on trial-averaged difference images.

Fig. 6A shows an example of the time course of response strength of orientation-difference images to four visual stimulus contrasts evaluated by the SD method, where the gray bar indicates the stimulus duration (8 s). The response level to the blank screen (in the 6.4 s before stimulus onset) remained about the same for all conditions. The ascending slopes and amplitude of optical responses increased systematically with stimulus contrast. The shape similarity of the response time courses was verified by normalizing the response amplitude frame by frame: at each time point, response amplitude to each contrast was divided by that for the maximal contrast (80%). Fig. 6B shows that the time courses of normalized amplitudes for each contrast reach and maintain a nearly constant level about 2.5 s after the onset of visual stimuli, which indicates that the time course of stimulus-driven response amplitudes are approximately contrast-invariant.

It makes sense to average the intrinsic optical signals across time and obtain a scalar contrast response function only if the spatial pattern of activated domains remains constant across time and if the pattern remains invariant across contrast levels (see Appendix). Preliminary evidence for the latter condition was shown in Figs. 3C and 5C, where averaged optical images for 4 tested contrasts were highly correlated with each other, but more detailed assessment was necessary. Consequently, we examined and compared the time courses of two kinds of spatial correlations, calculated only based on pixels from blood free zones within the ROI. Firstly, an "intra-contrast correlation" was calculated to assess separately for each contrast, the stability of the spatial pattern across time. Each image frame was correlated to a standard reference (average of the 20th–27th frames) for that contrast condition. As shown in Fig. 6C, the correlation coefficients rose to relatively high values (>0.8) by about 3 s after the onset of visual stimuli. This result indicates that, for a given contrast condition, a short time is needed to establish a stable spatial pattern, which is then maintained across the stimulus time course.

To further validate the contrast-invariance of the spatiotemporal response pattern, an "inter-contrast correlation" (Fig. 6D) was measured: at each time point, the difference image to the highest contrast was used as a reference image to correlate with those for other contrasts. Following stimulus onset, the "inter-contrast correlation" coefficient increased rapidly to a stable asymptote after about 2.5 s for each of the contrasts. Taken together, the time courses of the correlation coefficients in Figs. 6C and D confirm that, while briefly changing following the stimulus onset, the spatial pattern of optical responses becomes quite contrast- and time-invariant. Thus, within an appropriately chosen time window, response patterns can be further averaged across time and their strength can be adequately characterized by a scalar index (see Appendix).

The suitability of the data for further quantitative analysis of contrast response was evaluated from the above "inter-contrast correlation" analysis (Fig. 6D). Optical responses to the lowest contrast stimuli (10%) were the least well correlated with the highest contrast responses at each time point. Assuming stronger responses have higher statistical reliability, we therefore assessed the quality of each optical imaging dataset based on the correlation coefficient between responses to lowest and highest contrast stimuli. Only when the highest correlation coefficient between these responses (asterisks in Fig. 6D) was greater than 0.8 was the dataset used (e.g., in Fig. 6D, the highest such correlation coefficient, at the 19th frame, was 0.92). A time window of reliable data was defined as those frames having correlation coefficients within 10% of the maximum (e.g., in Fig. 6D, the 17–32nd frames, indicated by the pair of arrows) for each condition. This time window, which typically started at about the 20th frame (range 16–24th frame) and ended at about the 29th frame (range 26–32nd frame), was used for temporal averaging to obtain the average image for each condition to evaluate the strength of optical response, using the methods described earlier.

Contrast response functions from optical imaging

For orientation selective contrast response, orthogonally oriented drifting sinewave gratings at 4 contrasts (10%, 20%, 40% and 80%) were used as visual stimuli and the response images within the defined time window were averaged for each contrast. The spontaneous response of visual cortex (to the blank screen with average gray level) was evaluated from the pre-stimulus data (Presnaps, as discussed earlier, Fig. 1C). Contrast response functions were then normalized to vary from zero to unity. Figs. 7A–C show typical results from three animals, plotted as normalized contrast response functions assessed by SD (standard deviation of image intensity distribution, filled triangles), IQR (interquartile range of image intensity distribution, open triangles), and peak–trough difference (PT1, opened circles and PT2, filled circles) methods. The optical responses rise very rapidly with increasing stimulus contrast, typically reaching about half the maximal value when contrast is 10%.

Fig. 7D shows the average of normalized contrast response functions evaluated from all the valid orientation-difference optical image data ($N = 18$). For parametric characterization, the responses

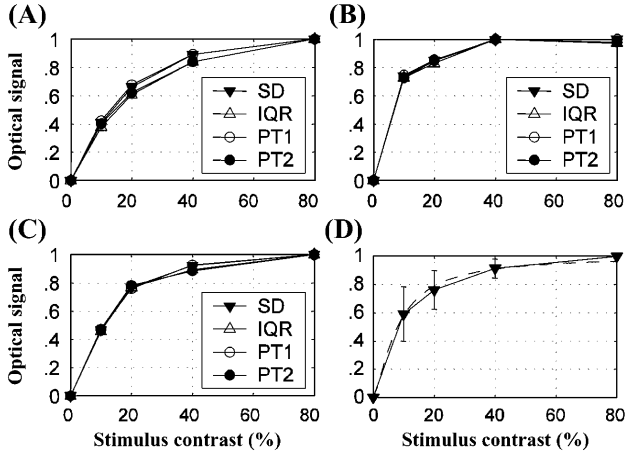

Fig. 7. CRFs for orientation selectivity assessed by optical imaging. (A–C) Typical contrast response functions for orientation, evaluated from 3 animals by SD, IQR, and PT methods; PT1 and PT2 show results from the most responsive sub-regions and from sub-maximally responsive sub-regions, respectively. (D) Averaged contrast response function (18 datasets from 8 animals), analyzed by the SD method (solid curve, error bar = standard deviation), fit with a Naka–Rushton function (dashed curve, C_{50} = 8.0%, k = 1.42, r^2 = 0.997).

were fit with a Naka–Rushton function (Albrecht and Hamilton, 1982; Sclar et al., 1990), $R = R_{max}\ C^k / (C^k + C_{50}^k) + M$, where R_{max} is the maximal response, C_{50} is the contrast at half-maximal response, and M represents the spontaneous response to zero contrast; both C_{50} and k jointly determine the shape and steepness of the contrast response function, though C_{50} has the greater impact. In practice, we used normalized differential CRF data, forcing R_{max} to unity and M to zero, leaving only two freely fitted parameters, k and C_{50}. The curve-fit for the average response in Fig. 7D is indicated by the dashed curve, where C_{50} = 8.0%, k = 1.42 (r^2 = 0.997).

Contrast response functions for direction selectivity were also evaluated from optical imaging data and are displayed in Fig. 8. Figs. 8A–C show contrast response functions from three datasets, presented in the same format as Fig. 7. The responses increased rapidly at low contrast, and at 10% contrast were about half the maximal response. Fig. 8D shows the average contrast response function for the valid datasets (N = 4). The fitted Naka–Rushton function is shown as a dashed curve, with best-fitting parameters C_{50} = 6.9% and k = 1.83 (r^2 = 0.999), which are similar to the values for orientation-difference data shown in Fig. 7.

Contrast response functions assessed from single unit recordings

Contrast response functions measured with single unit recording were estimated from the difference of average spike rates for correspondingly paired conditions (opposite directions of motion or orthogonal orientations). Examples of such CRFs for direction selectivity from 10 randomly selected neurons are shown in Fig. 9A. Most of them are monotonically increasing, with some saturation at high contrast levels. A few of the CRFs from the 43 valid datasets (DSI > 0.1) are non-monotonic, showing a decreased response at the highest contrast tested (Ledgeway and Baker, 2001). The average direction-selective contrast response function of these 43 neurons is shown in Fig. 9B (solid line and asterisks), which demonstrates an overall monotonic increasing

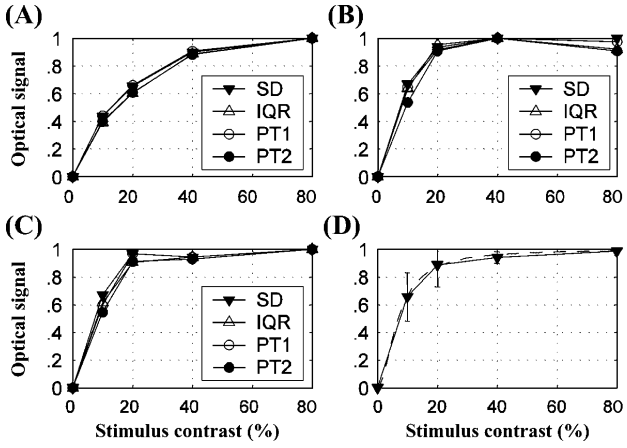

Fig. 8. CRFs for direction selectivity assessed by optical imaging. (A–C) Three contrast response functions for direction of motion, evaluated from 3 animals by SD, IQR, and PT methods; PT1 and PT2 show data from the most responsive sub-regions and from sub-maximally responsive sub-regions, respectively. (D) The averaged contrast response function (4 datasets from 3 animals) analyzed with the SD method (solid curve, error bar = standard deviation) fit with a Naka–Rushton function (dashed curve, C_{50} = 6.9%, k = 1.83, r^2 = 0.999).

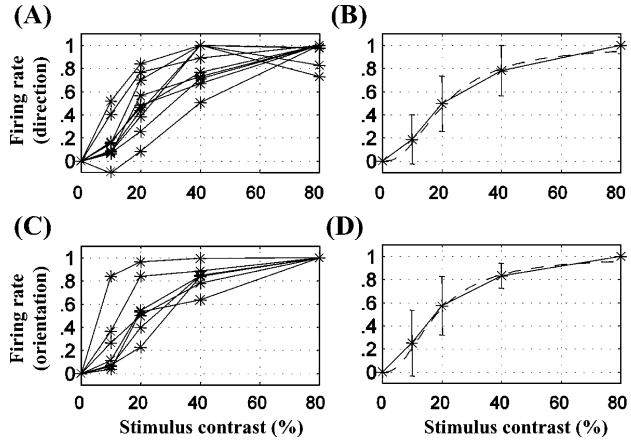

Fig. 9. Contrast response functions assessed from single unit recordings. (A) Ten examples of direction-selective contrast response functions (difference response to preferred and non-preferred stimuli) randomly chosen from 43 single unit recordings. Most neurons show monotonic increase in difference response (P − NP) with contrast, often with saturation at highest contrasts. (B) Average of all the normalized contrast response functions (solid line, error bar = standard deviation), and Naka–Rushton curve-fit (dashed curve, C_{50} = 20.3%, k = 2.13, r^2 = 0.995). (C) Seven contrast response functions for orientation selectivity from single unit recordings. (D) Average of normalized contrast response functions for orientation selectivity (solid line, error bar = standard deviation) with Naka–Rushton curve-fit (dashed curve, C_{50} = 17.3%, k = 2.06, r^2 = 0.997).

function with stimulus contrast. These data could be described by a Naka–Rushton function (dashed curve), with C_{50} of 20.3% and exponent k of 2.13 (r^2 = 0.995). Similarly, contrast response functions for orientation selectivity from 7 neurons are shown in Fig. 9C. The average of all the measured CRFs is shown in Fig. 9D (solid line and asterisks). A Naka–Rushton fit (dashed curve) indicates that the half-saturation contrast C_{50} is 17.3% and the exponent k is 2.06 (r^2 = 0.997).

The averaged CRFs measured by single unit recording for direction (Fig. 9B) and orientation selectivity (Fig. 9D) are quite similar, as shown by the comparable values of half saturation contrast C_{50} and exponent k. These averaged CRFs from single unit recording also agree reasonably well with those described in other studies (e.g., Albrecht and Hamilton, 1982; Lennie, 1998) but appear to be quite different from the CRFs evaluated from optical imaging data; both C_{50} and exponent k values for optical imaging data are lower (C_{50} = 8.0%, k = 1.42 for orientation and C_{50} = 6.9%, k = 1.83 for direction).

The effect of non-optimal stimuli on optical contrast response

In our single unit recordings, CRFs were measured with visual stimulus parameters such as spatial and temporal frequency optimized for each neuron. However, in optical imaging experiments, we measure population responses to paired sets of a single stimulus, which will inevitably be non-optimal for many of the contributing neurons. It is possible that sub-optimally responding neurons might have different CRFs than maximally responding neurons, contributing to a discrepancy between single unit recording and optical imaging. To investigate the effect of non-optimal stimulation on the optical contrast response function, we developed the peak–trough difference method (see Materials and methods, Figs. 3D–F and 5D–F) to

partition each orientation- or direction-map into sub-regions according to response strength and evaluate the contrast response functions from these sub-regions.

Fig. 10A shows 22 contrast response functions evaluated from the most responsive sub-regions (red and blue regions in Figs. 3F and 5F). Fig. 10B shows the average contrast response function (open circles and solid curve), which was fit with a Naka–Rushton function (C_{50} = 8.20%, k = 1.61, r^2=0.999). Fig. 10C shows the 22 corresponding contrast response functions evaluated from sub-maximally responsive sub-regions (orange and cyan regions in Figs. 3F and 5F). Fig. 10D shows the average contrast response function (open circles and solid curve), which was also well fit by a Naka–Rushton function (C_{50} = 8.22%, k = 1.58, r^2 = 0.999).

Effect of temporal parameters on single unit recordings

The optical responses were measured on a much slower time scale (stimuli of 8 s duration, separated by about 25 s inter-stimulus intervals, Fig. 1C) than the neurophysiological recordings (3 s duration, with ca. 1–2 s inter-stimulus intervals). If the contrast response function depended upon the temporal parameters with which it was measured, this might account for the difference in results from optical imaging and single unit recording. To investigate the possible effect of recording protocols, we measured CRFs on 7 neurons using temporal parameters matched to those used in optical imaging ("slow protocol", Fig. 11A), as well as conventionally ("fast protocol", Fig. 11C). Fig. 11B shows the average of the normalized CRFs in Fig. 11A (solid line and asterisks) and a Naka–Rushton curve-fit (dashed curve: C_{50} = 16.5%, k = 2.31, r^2 = 0.999). In a pair-wise comparison, the CRFs from the slow protocol almost always fell above the corresponding data from the fast protocol at low contrasts; thus the CRFs in panel C are systematically shifted downwards and to the right of those in panel A. Fig. 11D shows the average of the CRFs in Fig. 11C (solid line and asterisks) and the best-fitting Naka–Rushton function

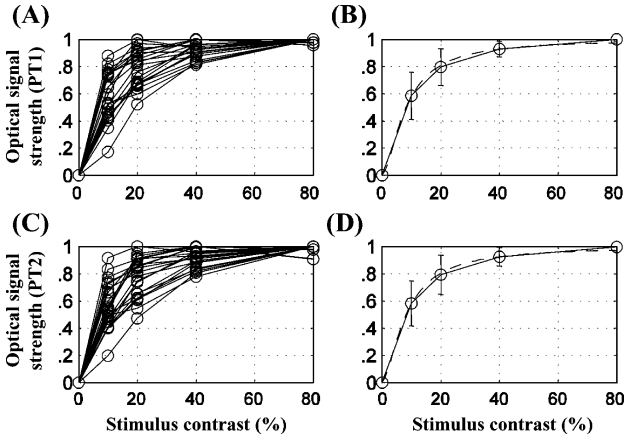

Fig. 10. CRFs from maximally and sub-maximally responsive sub-regions. (A) Twenty-two contrast response functions (CRFs) derived from maximally responsive sub-regions (see Figs. 3 and 5). (B) Average of CRFs in panel A (solid line, error bar = standard deviation) with Naka–Rushton function curve-fit (dashed curve, C_{50} = 8.20%, k = 1.61, r^2 = 0.999). (C) Twenty-two CRFs evaluated for sub-maximally responsive sub-regions. (D) Average of CRFs in panel C (solid line, error bar = standard deviation) with Naka–Rushton function curve-fit (dashed curve, C_{50} = 8.22%, k = 1.58, r^2 = 0.999).

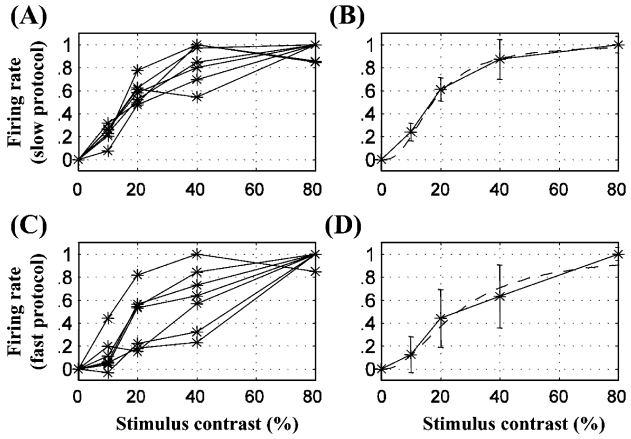

Fig. 11. CRFs from long- and short-time single unit recordings. (A) Contrast response functions from 7 neurons tested with temporal conditions mimicking those used in optical imaging measurements (8 s stimulus duration, about 25 s inter-trial interval). (B) Average of normalized contrast response functions (solid line; error bar = standard deviation) and a fitted Naka–Rushton function (dashed curve, C_{50} = 16.5%, k = 2.31, and r^2 = 0.999). (C) Corresponding contrast response functions of the same neurons in panel A, tested using conventional temporal conditions (3 s stimulus duration, short inter-trial interval). (D) Average of normalized contrast response functions in panel C (solid line; error bar = standard deviation). Naka–Rushton function (dashed curve) is fitted with C_{50} = 25.0%, k = 1.97, and r^2 = 0.972.

(dashed curve: C_{50} = 25.0%, k = 1.97, r^2 = 0.972). The lower C_{50} for the slow protocol confirms the appearance of a more pronounced saturation. However, this discrepancy of C_{50} between slow and fast protocols is much smaller than that between single units and optical imaging data. Furthermore, the k values for the slow protocols were more similar to those for the fast protocols than to those for optical imaging. Therefore, while the temporal parameters used in the measurements do have an effect on the CRFs, the effect is too small to account for the differences between optical and neurophysiological data.

The relationship between optical response and neural activity

From the previous analysis, we have seen that the contrast response functions evaluated for orientation and direction selectivity are quite different for optical imaging and for single units, as described by the half-saturation contrast level C_{50} and the steepness of the saturation related parameter k in the fitted Naka–Rushton functions. To examine the relationship between the optical and neural signals, we compared their response levels to the same 5 tested contrasts (blank, 10%, 20%, 40%, and 80%). Since the CRFs for orientation and direction selectivity were very similar, they were pooled for each type of signal (optical or electrophysiological). The averages of normalized CRFs from optical imaging (N = 22, open circles and solid line) and single units (N = 58, asterisks and solid line) are shown on the same graph in Fig. 12A. The optical imaging showed relatively stronger signals than would be expected by a linear proportionality from single units at low contrast levels; the signals half-saturate at different contrast levels, which was quantitatively confirmed by the Naka–Rushton curve-fits (dashed curve: C_{50} = 7.7%, k = 1.45 and r^2 = 0.998, for optical imaging data; dotted curve: C_{50}=18.0%, k=2.07 and r^2 = 0.996, for single units). The relative strength of the overall

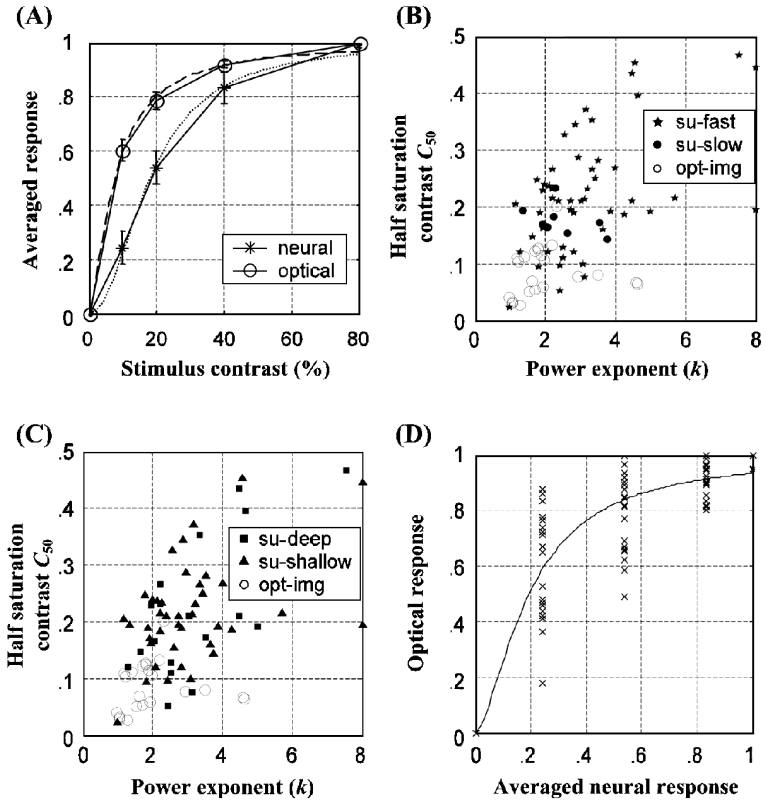

Fig. 12. Quantitative relationships between optical and neural responses. (A) Average CRFs evaluated from neural (solid line and asterisks) and optical (solid line and open circles) responses (error bar = standard error). The CRF for the optical signal is an average from both orientation- and direction-selective imaging data ($N = 22$), fit with a Naka–Rushton function (dashed curve, $C_{50} = 7.7\%$, $k = 1.46$, and $r^2 = 0.998$); the CRF for neural response is an average of single unit data ($N = 58$, for both direction and orientation selectivity), fit with a Naka–Rushton function (dotted curve, $C_{50} = 18.0\%$, $k = 2.07$, and $r^2 = 0.996$). (B) Fitted k and C_{50} values for individual single units from fast (★) and slow (•) recording protocols and individual optical imaging data (○). C_{50} and k values beyond the axis ranges are plotted on the top or right edges of the plot. These values for optical signals (○) segregate in the left-bottom corner and differ significantly from those for single units ($P = 1.42 \times 10^{-7}$ for C_{50} and $P = 0.003$ for k, two-tailed t test). (C) The same single units segregated into shallow (depth <1500 μm, ▲) and deep (■) groups, shown as scatterplot of fitted k and C_{50} values; shallow and deep neurons show no significant difference ($P = 0.869$ for C_{50} and $P = 0.660$ for k, two-tailed t test). (D) Scatterplot of optical responses against averaged neural response to 5 tested contrasts. The optical responses are related to the neural responses in a nonlinear manner, which can also be described with a Naka–Rushton function (half-saturation = 0.195, $k = 1.62$, and $r^2 = 0.989$).

neural activity in Fig. 12A is significantly lower than the optical signal strength at intermediate contrasts ($P < 0.005$ for 10% and 20% contrasts, one-tailed t test).

To explore in detail the difference between contrast response functions from the two kinds of measurement, we fit the CRFs of all the individual datasets from optical imaging and single unit recording with Naka–Rushton functions. Their half saturation and power exponent values are shown as scatterplots in Figs. 12B and C to assess two possible reasons for the different CRFs from single unit recording and optical imaging. Fig. 12B shows fitted k and C_{50} values for individual single units from fast (filled stars) and slow (filled circles) recording protocols. These parameters for optical signals (open circles) show less dispersion and segregate significantly from the single unit values for both slow and fast protocols ($P < 0.005$ for both k and C_{50}, two-tailed t test).

Another possible issue in the comparison between single unit and optical signal data is the effective depths of the two kinds of recording methods (see also Discussion). Neural contrast response might vary systematically with depth, while optical recording would be more indicative of shallow layer responses. However, our optical recordings utilized a relatively broad depth-of-field optical system and a longer wavelength, so they probably reflect activity from a wide range of depths. To examine whether neural contrast responses vary with depth, we partitioned our single unit data into two categories based on recording depth. Fig. 12C shows a scatterplot of fitted C_{50} and k values for neurons recorded at relatively shallow (<1500 μm, filled triangles) vs. greater depths (filled squares) in comparison to optical responses (open circles). The single unit C_{50} and k values for shallow versus deep recordings do not show a statistically significant difference ($P = 0.869$ for C_{50} and $P = 0.660$ for k, t test).

To describe the quantitative relationship between response strengths measured by optical and electrophysiological methods, a scatterplot of optical responses against the averaged single units' contrast response at the 5 examined contrast levels is shown in Fig. 12D. Note that the differential optical signal strength is nonlinearly related to the neural firing rate: the former is relatively more sensitive to low stimulus contrasts and shows greater saturation. It turns out that this nonlinear relationship can also be described by a Naka–Rushton function (smooth curve in Fig. 12D)—the optical response reaches half of its maximum when the neural response has reached only 19.5% of its maximum.

Discussion

We have quantified and compared the contrast response functions (CRFs) of neural populations by intrinsic optical signal imaging and single unit recording. Averaged CRFs from both differential optical signals and single units showed monotonically increasing responses with saturation at high contrasts. The quantitative relationship between the response levels of intrinsic optical signals and neural activity was nonlinear.

Quantification of optical response

We have considered three methods to quantify the strength of intrinsic optical signals. The standard deviation (SD) of the image pixel value distribution has been previously used as a measure of optical response strength (Schuett et al., 2001), which we have validated here by correlation analysis (Figs. 6C and D) and signal approximation theory (see Appendix). The results from correlation and approximation analysis also provide a basis for the inter-quartile range (IQR) and peak–trough difference (PT) methods.

Correlation analysis along the time course of visual response showed that the optical images stabilized into a temporal- and contrast-invariant spatial pattern (Figs. 6C and D). Though the time courses of response strength are complex (Fig. 6A) and vary from one dataset to another, they are of about the same shape for each contrast level within a dataset, as confirmed by the flatness of normalized response amplitudes (Fig. 6B) within a post-stimulus window (indicated by the pair of arrows in Fig. 6D). Therefore, the contrast response function is independent of the time point (within this window) at which it is measured—i.e., contrast-time separable, similar to that previously described for human BOLD fMRI (Boynton et al., 1996). Since the response spatial pattern is independent of contrast (the high correlation coefficients between responses to different contrast stimuli), the CRF is independent of pixel location. Taken together, these results indicate that the optical response is separable in its dependence on spatial location in the image, time lag (within the specified time window), and contrast level. This separability provides the basis for characterizing contrast response as a simple scalar function (see Appendix).

The SD and IQR methods have the advantage over PT that they do not require segmentation; however, their validity is contingent upon the nature and quality of the response images. As demonstrated by signal approximation, only highly correlated images are appropriate for these methods. Signals from large blood vessels have an aberrant temporal relation to the visual stimuli, and thus produce estimation errors of response strength by randomly skewing image intensity histograms; consequently, blood vessel regions were masked out of the difference-images for quantitative analysis. The adequacy of our blood vessel removal procedures was verified by the very small blank screen responses, the small correlation coefficient between optical signal to blank screen condition and stimulus-driven responses, and the high correlation between stimulus-activated optical signals (Figs. 3–6), validating the assumptions underlying the SD and IQR statistical methods. While SD can be applied for Gaussian-distributed data, IQR provides an alternative for non-Gaussian data, for example with systematically skewed histograms due to asymmetrical energy in the dark and light regions of optical difference images.

The PT method is more flexible for comparison of location-specific responses. For example in Fig. 10, we obtained CRFs from optimally and sub-optimally activated regions. Another advantage of PT is that, for noisy data, it provides unbiased amplitude estimation by canceling random noise from peak and trough subdomains, whereas the SD and IQR methods potentially lead to statistical bias (e.g., non-zero blank response, see Appendix).

Quantitative comparison of optical signals and neural firing

Although the CRFs from both optical signals and electrophysiology were evaluated in a comparable way and qualitatively similar monotonic, saturating functions, they differed significantly: the optical signals rose more steeply with contrast and saturated at a much lower contrast than the single unit responses, as shown by their different half-saturation contrasts (C_{50}) and power exponents (k) (Fig. 12). It was important to assess whether this difference arose from methodological factors rather than indicating a fundamental difference in the kinds of measurements. Possible sources of problems might arise from anatomical factors (contributions from A17 vs. A18, or from different laminae), relative optimality of stimuli, or differences in how visual stimuli were presented.

Conceivably, our A18 recordings might have been differentially contaminated by A17 responses in that the single unit recordings were clearly from A18, while the optical recordings were from a larger expanse of cortex which might have included some of A17. To ensure that our neural and optical recordings were from the same cortical region, we employed a craniotomy location (Tusa et al., 1979) as well as stimulus spatial and temporal frequency which were optimized for A18 (Issa et al., 2000; Movshon et al., 1978). Single unit recordings indeed showed low spatial/high temporal frequency preferences characteristic of A18; the spatial frequency employed for our optical recordings was optimal for A18. Reassuringly, clear optical responses tended to be always at the central area of our craniotomy, where our region of interest is located.

Another issue might be that optical recording reflects primarily superficial layer neural activity, while single units are from a wider range of depths which might have differing CRFs. Our single unit recordings were distributed randomly across laminae; taking care to get the best surface-zeroing possible, the estimated depth of our recordings ranged from 120 to 3420 μ (1426 ± 721 μ). Additionally, we did not find significant differences in average neural CRFs from the full set of data ($N = 58$) and from a subset of neurons ($N = 40$) recorded at superficial depths (less than 1500 μ). Since we used a wide depth-of-field optical system (f2.5) rather than a high-NA macroscope (Grinvald et al., 1999) and a long illumination wavelength (720 nm), our optical recordings sampled across a wider range of laminae. Therefore, it seems unlikely that our optical measurements systematically sampled a significantly different range of depths than the neurophysiology.

In optical imaging, only one set of visual stimulus parameters is employed, which will inevitably be non-optimal for many of the neurons contributing to the response. The high correlations between responses to different contrasts (Fig. 6) imply a spatial uniformity of CRFs evaluated from differential optical signals, consistent with the response intensity partition analysis (Fig. 10) showing no difference in shape of the CRFs between pixels within optimally and sub-optimally stimulated sub-regions. Carandini and Sengpiel (2004) also found a similar uniformity using a different data processing protocol, which was designed to detect differences in contrast response functions of different pixels. This result is also consistent with neurophysiological studies showing that the shape

of a given neuron's contrast response function is invariant to non-optimal stimulus parameters (e.g., Albrecht and Hamilton, 1982; Sclar and Freeman, 1982). Although the spatial uniformity of optical responses might be due to the limited resolution of optical imaging, this uniformity facilitates comparison of optical responses to neural firing rates: rather than compare the two kinds of responses location by location, we can simply compare the average optical responses to averaged neural firing rates.

Another methodological difference is that usually a relatively short stimulus duration (3 s) and minimal inter-trial interval were used for electrophysiology, unlike the protocol for optical imaging (Fig. 1) involving much longer times for each trial. To address the possibility that this difference might have affected the quantitative comparison of CRFs, some neurons were recorded with time parameters designed to mimic those used for optical imaging. While CRFs from this slow protocol were somewhat closer to those from optical imaging (Fig. 11), this effect was too small to account for the large difference between optical imaging and single units (Fig. 12B).

Possible origin of the nonlinearity and its implications for neuroimaging

Intrinsic optical signals reflect biophysical effects including blood oxygenation and neuronal swelling (Blasdel, 1997; Grinvald et al., 1999; Rodriguez et al., 2001), which originate from changes in a series of physiological phenomena including neurotransmitter levels, ion-channel activities, membrane potentials, firing rates, and consequently, the local field potential, blood flow, and metabolic rate (Lauritzen and Gold, 2003; Logothetis, 2003; Magistretti and Pellerin, 1999; Rothman et al., 2003). Blood flow and glucose uptake are coupled to neurotransmission and ion channel activity to satisfy local energy requirements (Hyder et al., 2002; Parri and Crunelli, 2003; Schwartz et al., 1979; Zonta et al., 2003). Energy consumption can be linearly related to firing rate (Smith et al., 2002); however blood oxygenation may be coupled (Jones et al., 2001; Mechelli et al., 2001) or decoupled (Mathiesen et al., 1998; Mintun et al., 2001; Norup Nielsen and Lauritzen, 2001) with blood flow. Oxygenation and change of blood flow have different time courses (Vanzetta and Grinvald, 1999), with blood deoxygenation normally preceding blood flow increase by more than 1 s (Malonek et al., 1997); thus local oxygenation level can change over time even when electrical activity remains unchanged. Other factors complicating the neural–hemodynamic coupling are threshold effects for change of blood flow (Norup Nielsen and Lauritzen, 2001) and effects of anesthetic state (Shulman et al., 1999; Vanzetta and Grinvald, 1999). While the membrane activity of neuron populations, which forms the basis of local field potentials, may be more closely related to oxygenation signals (Logothetis et al., 2001), average neural firing is an anesthesia-dependent sigmoidal function of local field potential (Eeckman and Freeman, 1991). Taken together, the nature of these interactions determines the ultimate relationship between neuro-imaging signals and neural firing rates.

The relationship of BOLD fMRI to neural firing is a question of much interest (e.g., Logothetis, 2003; Scannell and Young, 1999). Our results are potentially relevant to fMRI, since the optical signal is a similarly slow hemodynamically driven signal which in part reflects blood oxygenation levels. Meanwhile, we would point out two caveats regarding this comparison. Firstly, at the wavelength of 720 nm used here, optical signals could reflect changes in blood oxygenation as well as light scattering (Blasdel, 1997; Grinvald et al., 1999; Rodriguez et al., 2001). However, the similarly slow time course of all these changes suggests that they are all hemodynamically driven, and thus comparable in origin (Malonek and Grinvald, 1996; Vanzetta and Grinvald, 1999). A second caveat is that the quantitative relation between our optical and electrophysiological response strengths was derived from a differential protocol. Because of the nonlinear relationship which we have demonstrated, a comparison of differential maps to differential neural responses is quantitatively comparable only to differential fMRI, but not necessarily to imaging responses measured against blank-condition baselines (single condition responses, such as those of Logothetis et al., 2001). Differential images contain only stimulus-specific responses, whereas single condition images additionally contain a substantial stimulus-nonspecific component ("global signal"—Grinvald et al., 1999). The presence of a stimulus-nonspecific component would greatly complicate any comparison to visually-driven neural activity, since locations without neural response would exhibit a non-zero imaging signal. Our results suggest that fMRI responses, when measured in a differential protocol (Kim et al., 2000), might also be subject to a similar nonlinear relationship.

Our optical comparison between CRFs demonstrates that optical signals are nonlinearly related to neuronal firing. At low response levels, this nonlinearity resembles the relationship between membrane potential and neuronal population firing rates (Eeckman and Freeman, 1991): membrane potential (like optical response) is larger than would be expected from a linear proportionality with firing rate. This disproportionality is consistent with the suggestion that hemodynamic signals might be more sensitive to weak activity from a large neuron population (Scannell and Young, 1999) and also with the idea that intrinsic optical signals are sensitive to not only firing rates but also subthreshold activities (Das and Gilbert, 1995; Masino, 2003; Toth et al., 1996).

Acknowledgments

This work was supported by a Canadian Institutes of Health Research grant MA-9685 to CLB. We thank Rhone-Poulenc Rorer for donation of Gallamine triethiodide. We also thank Lynda Domazet, Aaron Johnson, and Yuning Song for assistance with the experiments, and the staff at InstruTech Corp. for their help with the DVP image processor. We are grateful for advice on optical imaging techniques from Ehud Kaplan, Harry Orbach, and Nicholas Swindale and particularly David Fitzpatrick and members of his laboratory. We also thank Serge Dumoulin for comments on the manuscript. We also gratefully thank two anonymous reviewers for critical suggestions and the editors for their help.

Appendix A

Here, we present a more rigorous basis for two key aspects of quantifying the amplitude of differential optical signals based on signal approximation. Firstly, the high correlation coefficient between activated patterns and the low noise for the blank condition are necessary precursors for CRF evaluation. We also show that the differential optical signal is roughly space–time-contrast separable.

A.1. Characterizing image signals and evaluating the optical response strength

The strength of optical response across the spatial extent of an image resembles the altitude variation of a three-dimensional surface. Because of the complexity of the surface geometry, the characterization of such surface data is challenging, and its quantitative comparison across a series of conditions is even more difficult. Based upon previous studies in characterizing surface data (Dong et al., 1992, 1994; Nowicki, 1985) and the similarity of the optical response patterns to different stimulus contrasts, we combine image signal approximation and correlation analysis to derive a more rigorous basis for a statistical representation (SD and IQR) for optical response strength.

Suppose differential images $I_1(x, y)$ and $I_2(x, y)$ within an arbitrarily shaped region of interest (ROI, N pixels) are reshaped into zero-mean one-dimensional vectors V_1 and V_2, respectively. If these images are similar in spatial pattern, then one can be expressed as a linear approximation of the other, with error vector $\vec{e}$:

$$V_1 = a_{12}V_2 + \vec{e} \tag{1}$$

where

$$V_1 = [v_1(1)\ v_1(2)...v_1(i)...v_1(N)] \tag{2}$$

$$V_2 = [v_2(1)\ v_2(2)...v_2(i)...v_2(N)] \tag{3}$$

$$\vec{e} = [e(1)\ e(2)...e(i)...e(N)] \tag{4}$$

The optimal approximation coefficient a_{12} minimizes the summed square errors

$$\varepsilon = ||\vec{e}||_2^2 = \sum_{i=1}^{N}[v_1(i) - a_{12}v_2(i)]^2 \tag{5}$$

or in continuous form

$$\varepsilon = ||e(t)||_2^2 = \int [V_1(t) - a_{12}V_2(t)]^2 dt \tag{6}$$

A minimum is achieved when

$$\frac{d\varepsilon}{da_{12}} = \frac{d}{da_{12}}\int [V_1(t) - a_{12}V_2(t)]^2 dt = 0 \tag{7}$$

yielding

$$a_{12} = \frac{\int V_1(t)V_2(t)dt}{\int V_2^2(t)dt} \text{ or in discrete form } a_{12} = \frac{\sum_i v_1(i)v_2(i)}{\sum_i v_2^2(i)} \tag{8}$$

Substituting Eq. (8) into Eq. (5) using the discrete form, the minimized approximation error is

$$\tilde{\varepsilon}_{\min} = \frac{\varepsilon_{\min}}{\sum_i v_1^2(i)} = 1 - \frac{\left[\sum_i v_1(i)v_2(i)\right]^2}{\sum_i v_1^2(i)\ \sum_i v_2^2(i)} \equiv 1 - r^2 \tag{9}$$

where

$$r = \frac{\sum_i v_1(i)v_2(i)}{\sqrt{\sum_i v_1^2(1)\ \sum_i v_2^2(i)}} \tag{10}$$

is the correlation coefficient of the two optical images.

Eq. (9) links the correlation coefficient r with the approximation of two signals, in which a larger r corresponds to a smaller approximation error. If r is sufficiently large, the two signals can be considered linearly dependent and having the same shape of intensity histograms; the relative optical response strength can then be represented by the approximation coefficient a_{12}, which can be characterized by a suitable histogram shape parameter, such as the standard deviation (SD) or the interquartile range (IQR) of the intensity dispersion.

Stimulus-driven images with high correlation coefficients have similar intensity histograms (Figs. 3–5), indicating the pixel intensities in each image to different contrasts systematically change by a constant scale factor, which provides a scalar metric of contrast response strength. High correlation coefficients between stimulus-driven response images are necessary but not sufficient to obtain a CRF from differential optical signals; the validity of this measure also rests upon the negligibility of response strength (SD) to the blank condition to avoid potential bias in the response strength estimation.

We suppose the measured signal (N pixel vector V_m) is a combination of cortical responses (V_c) and additive zero-mean noise (n). Because the mean of the optical difference-image response is also zero,

$$\begin{aligned}\text{var}(V_m) &= E[(V_c + n)^2] - E[V_c + n]^2 \\ &= E\left[\left(V_c^2 + 2V_c \cdot n + n^2\right)\right]\end{aligned} \tag{11}$$

where $E[.]$ indicates the expectation. Since the noise is uncorrelated with the cortical response (Figs. 3–5C),

$$\text{SD}(V_m) = (\text{var}(V_m))^{1/2} = \left(E\left[V_c^2\right] + E\left[n^2\right]\right)^{1/2} \tag{12}$$

$E[n^2]$ produces a bias for signal strength estimation by the SD method; furthermore, its effect will interact with the cortical response V_c, thereby distorting the shape of the estimated CRF. Therefore, in additional to high correlation between stimulus-driven optical responses, a negligible blank response is also a necessary condition for validity of the SD and IQR method.

A.2. "Space–time-contrast separability" of optical response strength

Although contrast invariance of single neuron orientation selectivity is well known, it does not necessarily imply contrast invariance for optical signals, where each pixel contains many neurons (Carandini and Sengpiel, 2004). Because we do not know the exact coupling relation between neural activity and optical signals, an arbitrary weighing factor w is introduced to relate these two variables as follows. Consider the intensities of the i-th pixel in two images V_1 and V_2 as indicated in Eqs. (2) and (3), $v_1(i)$ and $v_2(i)$, which reflect the activities of K neurons within a small area on the cortical surface under two contrast stimulus conditions, respectively:

$$v_1(i) = \sum_j^K s_1(j)w_1(i,j) \text{ and } v_2(i) = \sum_j^K s_2(j)w_2(i,j) \tag{13}$$

where $s_1(j)$ and $s_2(j)$ represent responses of the j-th neuron under conditions 1 and 2; $w_1(i,j)$ and $w_2(i,j)$ are the weights with which

the j-th neuron contributes to the i-th pixel under the two corresponding conditions. We can represent the pixel value $v_1(i)$ by $v_2(i)$ without further assumption as

$$\sum_{j}^{K} s_1(j)w_1(i,j) \approx b_{12}(i) \cdot \sum_{j}^{K} s_2(j)w_2(i,j) \quad (14)$$

Because the response properties (e.g., CRFs) vary from neuron to neuron and the coupling weight $w(i, j)$ between electrophysiology and intrinsic optical signals could also vary for different neurons, $b_{12}(i)$ might vary with pixel position. A high correlation coefficient between spatial patterns of optical response is obtained if $b_{12}(i)$ in Eq. (14) is a constant; in that case it is equal to a_{12} in Eq. (1), which is independent of the pixel position (i). This constancy of b_{12} across space is consistent with the uniformity of optical CRFs reported in cat A17 (Carandini and Sengpiel, 2004).

Though the time courses of optical responses (e.g., Fig. 6A) are complex and vary from one dataset to another, the normalized response of a given dataset (Fig. 6B) becomes time-independent (flat) over some time-window following stimulus onset (gray bar in Fig. 6D). Therefore, the time course of the optical response can be characterized by a function $S(t)$, which is contrast-invariant (to within a scale factor); the contrast response function $F(c, x, y)$ can in principle be estimated by the response values (Fig. 6B) at any time point within the defined time-window. Furthermore, Eq. (14) indicates function $F(c, x, y)$ is independent of spatial position (x, y). Thus, optical response strength $R(x, y, t, c)$ can be considered as a separable function of pixel location (x, y), time (t), and stimulus contrast (c) and expressed as:

$$R(x,y,t,c) = P(x,y)S(t)F(c) \quad (15)$$

i.e., showing the intrinsic optical signal separately depends upon the spatial pattern of response across the cortical surface, $P(x, y)$ (e.g., orientation or direction map), the time course of optical response, $S(t)$, and a scalar contrast response function, $F(c)$.

References

Albrecht, D.G., Hamilton, D.H., 1982. Striate cortex of monkey and cat: contrast response function. J. Neurophysiol. 48, 217–237.

Albrecht, D.G., Geisler, W.S., Frazor, R.A., Crane, A.M., 2002. Visual cortex neurons of monkeys and cats: temporal dynamics of the contrast response function. J. Neurophysiol. 88, 888–913.

Anderson, J.S., Lampl, I., Gillespie, D.C., Ferster, D., 2000. The contribution of noise to contrast invariance of orientation tuning in cat visual cortex. Science 290, 1968–1972.

Blasdel, G.G., 1997. Strategies of visual perception suggested by optically imaged patterns of functional architecture in monkey visual cortex. Ann. N. Y. Acad. Sci. 820, 170–195.

Bonds, A.B., 1991. Temporal dynamics of contrast gain in single cells of the cat striate cortex. Vis. Neurosci. 6, 239–255.

Bonhoeffer, T., Grinvald, A., 1993. The layout of iso-orientation domains in area 18 of cat visual cortex: optical imaging reveals a pinwheel-like organization. J. Neurosci. 13, 4157–4180.

Boynton, G.M., Engel, S.A., Glover, G.H., Heeger, D.J., 1996. Linear system analysis of functional magnetic resonance imaging in human V1. J. Neurosci. 16, 4207–4221.

Brainard, D.H., 1997. The psychophysics toolbox. Spat. Vis. 10, 433–436.

Carandini, M., Sengpiel, F., 2004. Contrast invariance of functional maps in cat primary visual cortex. J. Vis. 4, 130–143.

Das, A., Gilbert, C.D., 1995. Long-range horizontal connections and their role in cortical reorganization revealed by optical recording of cat primary visual cortex. Nature 375, 780–784.

Dong, W.P., Sullivan, P.J., Stout, K.J., 1992. Comprehensive study of parameters for characterizing three-dimensional surface topography I: some inherent properties of parameter variation. Wear 159, 161–171.

Dong, W.P., Sullivan, P.J., Stout, K.J., 1994. Comprehensive study of parameters for characterizing three-dimensional surface topography III: parameters for characterizing amplitude and some functional properties. Wear 178, 29–43.

Eeckman, F.H., Freeman, W.J., 1991. Asymmetric sigmoid non-linearity in the rat olfactory system. Brain Res. 557, 13–21.

Grinvald, A., Shoham, D., Shmuel, A., Glaser, D., Vanzetta, I., Shtoyermann, E., Slovin, H., Sterkin, A., Wijnbergen, C., Hildesheim, R., Arieli, A., 1999. In-vivo optical imaging of cortical architecture and dynamics. In: Windhorst, U., Johansson, H. (Eds.), Techniques in Neuroscience Research. Springer Verlag, pp. 893–969.

Hanson, S.J., Bly, B.M., 2001. The distribution of BOLD susceptibility effects in the brain is non-Gaussian. NeuroReport 12, 1971–1977.

Heeger, D.J., Huk, A.X., Geisler, W.S., Albrecht, D.G., 2000. Spikes versus BOLD: what does neuroimaging tell us about neuronal activity? Nat. Neurosci. 3, 631–633.

Hyder, F., Rothman, D.L., Shulman, R.G., 2002. Total neuroenergetics support localized brain activity: implications for the interpretation of fMRI. Proc. Natl. Acad. Sci. U. S. A. 99, 10771–10775.

Issa, N.P., Trepel, C., Stryker, M.P., 2000. Spatial frequency maps in cat visual cortex. J. Neurosci. 20, 8504–8514.

Jones, M., Berwick, J., Johnston, D., Mayhew, J., 2001. Concurrent optical imaging spectroscopy and laser-Doppler, flowmetry: the relationship between blood flow, oxygenation, and volume in rodent barrel cortex. NeuroImage 13, 1002–1015.

Kim, D.S., Duong, T.Q., Kim, S.G., 2000. High-resolution mapping of iso-orientation columns by fMRI. Nat. Neurosci. 3, 164–169.

Lauritzen, M., Gold, L., 2003. Brain function and neurophysiological correlates of signals used in functional neuroimaging. J. Neurosci. 23, 3972–3980.

Ledgeway, T., Baker Jr., C.L., 2001. A neurometric function analysis of the direction selectivity of visual cortex neurons as a function of stimulus contrast. Soc. Neurosci. Abstr. 164.3.

Lennie, P., 1998. Single units and visual cortical organization. Perception 27, 889–935.

Logothetis, N.K., 2003. The underpinnings of the BOLD functional magnetic resonance imaging signal. J. Neurosci. 23, 3963–3971.

Logothetis, N.K., Pauls, J., Augath, M., Trinath, T., Oeltermann, A., 2001. Neurophysiological investigation of the basis of the fMRI signal. Nature 412, 150–157.

Magistretti, P.J., Pellerin, L., 1999. Cellular mechanisms of brain energy metabolism and their relevance to functional brain imaging. Philos. Trans. R. Soc. London, B Biol. Sci. 354, 1155–1163.

Malonek, D., Grinvald, A., 1996. Interaction between electrical activity and cortical microcirculation revealed by imaging spectroscopy: implications for functional brain mapping. Science 272, 551–554.

Malonek, D., Dirnagl, U., Lindauer, U., Yamada, U., Kanno, I., Grinvald, A., 1997. Vascular imprints of neuronal activity: relationships between the dynamics of cortical blood flow, oxygenation, and volume changes following sensory stimulation. Proc. Natl. Acad. Sci. U. S. A. 94, 14826–14831.

Mareschal, I., Baker Jr., C.L., 1999. Cortical processing of second-order motion. Vis. Neurosci. 16, 527–540.

Masino, S.A., 2003. Quantitative comparison between functional imaging and single-unit spiking in rat somatosensory cortex. J. Neurophysiol. 89, 1702–1712.

Mathiesen, C., Caesar, K., Akgoren, N., Lauritzen, M., 1998. Modification of activity-dependent increases of cerebral blood flow by excitatory synaptic activity and spikes in rat cerebellar cortex. J. Physiol. (London) 512, 555–566.

Mechelli, A., Price, C.J., Friston, K.J., 2001. Nonlinear coupling between evoked rCBF and BOLD signals: a simulation study of hemodynamic responses. NeuroImage 14, 862–872.

Mintun, M.A., Lundstrom, B.N., Snyder, A.Z., Vlassenko, A.G., Shulman, G.L., Raichle, M.E., 2001. Blood flow and oxygen delivery to human brain during functional activity: theoretical modeling, and experimental data. Proc. Natl. Acad. Sci. U. S. A. 98, 6859–6864.

Movshon, J.A., Thompson, I.D., Tolhurst, D.J., 1978. Spatial and temporal contrast sensitivity of neurons in areas 17 and 18 of the cat's visual cortex. J. Physiol. (London) 283, 101–120.

Norup Nielsen, A., Lauritzen, M., 2001. Coupling and uncoupling of activity-dependent increase of neural activity and blood flow in rat somatosensory cortex. J. Physiol. (London) 533, 773–785.

Nowicki, B., 1985. Multiparameter representation of surface roughness. Wear 102, 161–176.

Parri, F., Crunelli, V., 2003. An astrocyte bridge from synapse to blood flow. Nat. Neurosci. 6, 5–6.

Payne, B.R., Peters, A., 2002. The cat primary visual cortex. Academic Press, San Diego.

Pelli, D.G., 1997. The VideoToolbox software for visual psychophysics: transforming numbers into movies. Spat. Vis. 10, 437–442.

Rees, G., Friston, K., Koch, C., 2000. A direct quantitative relationship between the functional properties of human and macaque V5. Nat. Neurosci. 3, 716–723.

Rothman, D.L., Behar, K.L., Hyder, F., Shulman, R.G., 2003. In vivo NMR studies of the glutamate neurotransmitter flux and neuroenergetics: implications for brain function. Annu. Rev. Physiol. 65, 401–427.

Rodriguez, J., Xiao, F., Ferrara, D., Ewing, J., Zhang, S., Alexander, S., Battarbee, H., 2001. Implementation of near-infrared spectroscopy in a rat model of cardiac arrest and resuscitation. In: Tuchin, V.V. (Ed.), Proc. SPIE Vol. 4707, Saratov Fall Meeting 2001: Optical Technologies in Biophysics and Medicine III, pp. 83–91.

Scannell, J.W., Young, M.P., 1999. Neuronal population activity and functional imaging. Proc. R. Soc. London, B Biol. Sci. 266, 875–881.

Schwartz, W.J., Smith, C.B., Davidsen, L., Savaki, H., Sokoloff, L., Mata, M., Fink, D., Gainer, H., 1979. Metabolic mapping of functional activity in the hypothalamo–neurohypophysial system of the rat. Science 205, 723–725.

Schuett, S., Bonhoeffer, T., Hubener, M., 2001. Pairing-induced changes of orientation maps in cat visual cortex. Neuron 32, 325–337.

Sclar, G., Freeman, R.D., 1982. Orientation selectivity in the cat's striate cortex is invariant with stimulus contrast. Exp. Brain Res. 46, 457–461.

Sclar, G., Maunsell, J.H.R., Lennie, P., 1990. Coding of image contrast in central visual pathways of the macaque monkey. Vision Res. 30, 1–10.

Shmuel, A., Grinvald, A., 1996. Functional organization for direction of motion and its relationship to orientation maps in cat area 18. J. Neurosci. 16, 6945–6964.

Shulman, R.G., Rothman, D.L., Hyder, F., 1999. Stimulated changes in localized cerebral energy consumption under anesthesia. Proc. Natl. Acad. Sci. U. S. A. 96, 3245–3250.

Smith, A.J., Blumenfeld, H., Behar, K.L., Rothman, D.L., Shulman, R.G., Hyder, F., 2002. Cerebral energetics and spiking frequency: the neurophysiological basis of fMRI. Proc. Natl. Acad. Sci. U. S. A. 99, 10765–10770.

Swindale, N.V., Matsubara, J.A., Cynader, M.S., 1987. Surface organization of orientation and direction selectivity in cat area 18. J. Neurosci. 7, 1414–1427.

Thompson, J.K., Peterson, M.R., Freeman, R.D., 2003. Single-neuron activity and tissue oxygenation in the cerebral cortex. Science 299, 1070–1072.

Toth, L.J., Rao, S.C., Kim, D.S., Somers, D., Sur, M., 1996. Subthreshold facilitation and suppression in primary visual cortex. Proc. Natl. Acad. Sci. U. S. A. 93, 9869–9874.

Tusa, R.J., Rosenquist, A.C., Palmer, L.A., 1979. Retinotopic organization of area 18 and 19 in the cat. J. Comp. Neurol. 185, 657–678.

Vanzetta, I., Grinvald, A., 1999. Increased cortical oxidative metabolism due to sensory stimulation: implications for functional brain imaging. Science 286, 1555–1558.

Weliky, M., Bosking, W.H., Fitzpatrick, D., 1996. A systematic map of direction preference in primary visual cortex. Nature 379, 725–728.

Zhan, C., Ledgeway, T., Baker, C.L. Jr., 2002. Optical imaging of contrast-dependent direction selectivity in visual cortex. Soc. Neurosci. Abstr. 657.4.

Zhou, Y.X., Baker Jr., C.L., 1996. Spatial properties of envelope-responsive cells in area 17 and 18 neurons of the cat. J. Neurophysiol. 75, 1038–1050.

Zonta, M., Angulo, M.C., Gobbo, S., Rosengarten, B., Hossmann, K.A., Pozzan, T., Carmignoto, G., 2003. Neuron-to-astrocyte signaling is central to the dynamic control of brain microcirculation. Nat. Neurosci. 6, 43–50.